Supplemental Document

Optics Letters

Efficient misalignment correction for annular LED arrays in intensity diffraction tomography: supplement

RUIZHI ZHU,[1,2,†] WENJIE ZOU,[1,2,†] RUNNAN ZHANG,[1,2] ZIHAO ZHOU,[1,2] JIASONG SUN,[1,2] QIAN CHEN,[2] NING ZHOU,[1,2,3] AND CHAO ZUO[1,2,*]

[1] *Smart Computational Imaging Laboratory (SCILab), Nanjing University of Science and Technology, Nanjing, Jiangsu 210094, China*
[2] *Jiangsu Key Laboratory of Spectral Imaging & Intelligent Sense, Nanjing, Jiangsu 210094, China*
[3] *zhouning@njust.edu.cn*
[†] *These authors contributed equally to this work.*
[*] *zuochao@njust.edu.cn*

Supplement DOI: https://doi.org/10.6084/m9.figshare.28675976

Parent Article DOI: https://doi.org/10.1364/OL.557164

Efficient misalignment correction for annular LED arrays in intensity diffraction tomography: supplemental document

This document provides supplementary information for “Efficient misalignment correction for annular LED arrays in intensity diffraction tomography”.

1. ANALYSIS OF NOISE RESISTANCE OF PC AND NCC IN THE WAVELENGTH CALIBRATION OF THE MCIDT ALGORITHM

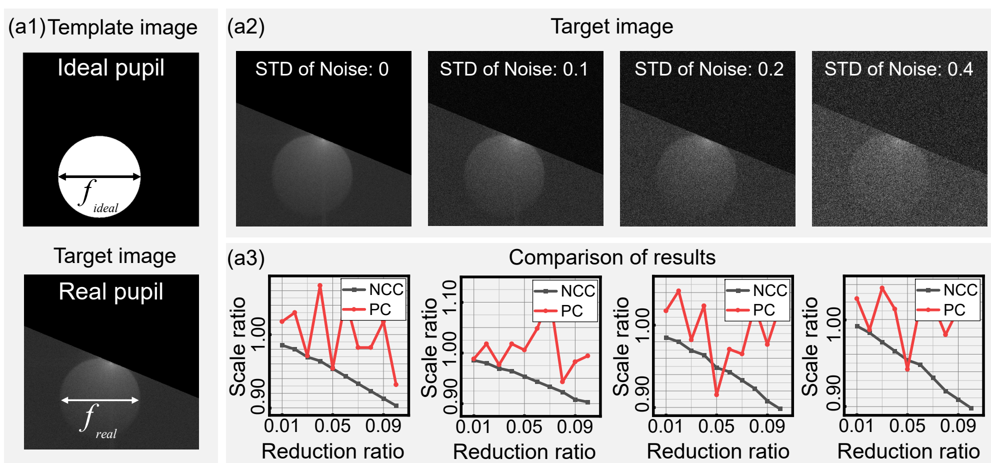

Fig. S1. Analysis of noise resistance of PC and NCC in the wavelength calibration of the efficient misalignment correction method for annular LED arrays in IDT (mcIDT). (a1) Template image and target image. (a2) Target images with varying levels of Gaussian noise. (a3) Comparison of computational results between PC and NCC algorithms.

To verify the necessity of substituting the normalized cross-correlation (NCC) algorithm for the traditional phase correlation (PC) algorithm in the improved Fourier-Mellin Transform (FMT) algorithm during light source wavelength calibration, we conducted a simulation comparison using both algorithms. As shown in Fig. S1(a1), we used the ideal pupil from the reconstruction algorithm as the template image. We added Gaussian noise with different standard deviations (STD) to the two-dimensional (2D) spectrum of the actual captured image to generate the target images for calibration. Subsequently, for these target images with varying noise levels, we gradually reduced the scaling ratio from 0.99 to 0.9 in steps of 0.01 (corresponding to an actual wavelength change from 522 nm to 575 nm), as shown in Fig. S1(a2). We then used both the improved FMT algorithm and the traditional FMT algorithm to correct the scaling ratio between the template image and the target images, obtaining the calibration results under different noise levels, as shown in Fig. S1(a3). The comparison results indicate that, due to the presence of noise in the 2D spectrum of the actual captured image, the impact of noise is further amplified after the logarithmic polar coordinate transformation, rendering the PC algorithm incapable of accurately calculating the scaling ratio. In contrast, even after the addition of Gaussian noise, the NCC algorithm can still ensure stable and accurate calibration, meeting the requirements for preliminary light-emitting diode (LED) wavelength calibration. Therefore, the substitution of the NCC algorithm for the PC algorithm in the proposed improved FMT method to achieve preliminary wavelength calibration is highly effective.

2. WORKFLOW OF THE IMPROVED FMT ALGORITHM

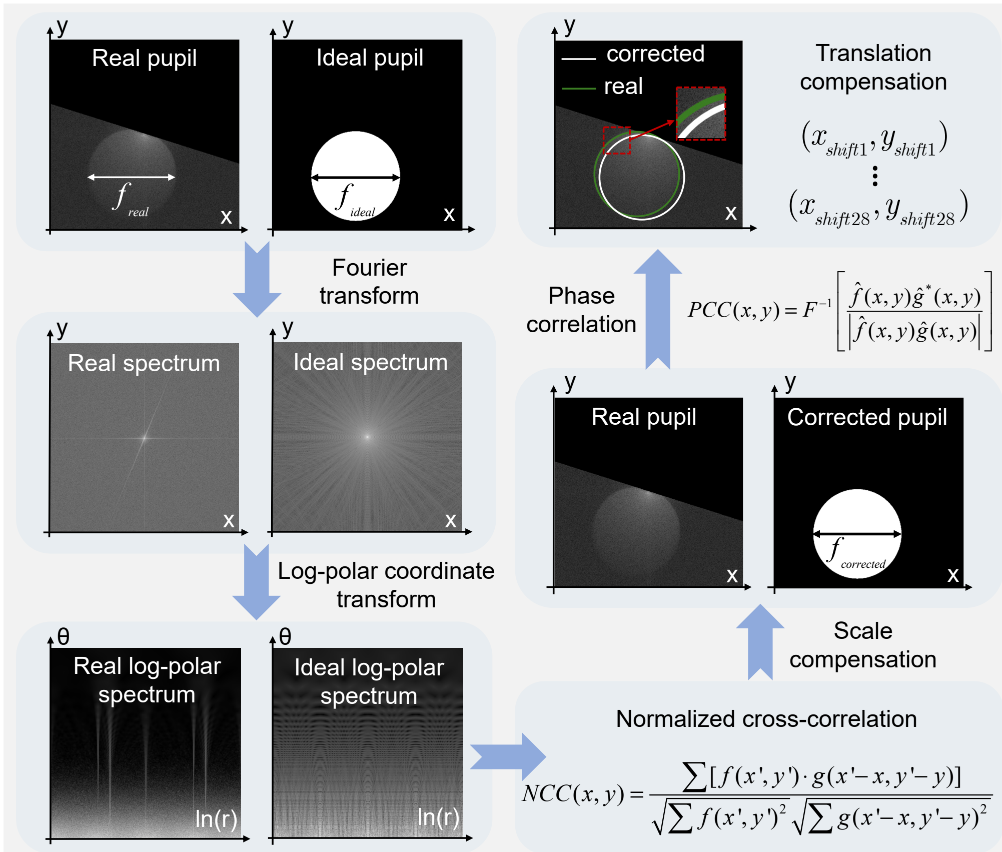

Fig. S2. Workflow of the Improved FMT algorithm.

Figure S2 provides a detailed illustration of the workflow of the improved FMT algorithm [1, 2]. Initially, Fourier transforms are applied to both the actual and ideal pupil images. Prior to image registration, filtering and noise reduction operations are performed to enhance the accuracy of the calibration. Then, the images are transformed into logarithmic polar coordinate images. With the center of the frequency domain image as the origin(x_0, y_0), each point (x, y) in the frequency domain can be transformed into the log-polar coordinate system $(\ln(r), \theta)$ [3], and the log-polar coordinate image is obtained by:

$$\begin{cases} r = \sqrt{(x-x_0)^2 + (y-y_0)^2} \\ \theta = \arctan(\frac{y-y_0}{x-x_0}) \end{cases} \tag{S1}$$

Subsequently, the images transformed into log-polar coordinates are subjected to NCC operations, with the formula as follows [4]:

$$NCC(x,y) = \frac{\sum[f(x',y') \cdot g(x'-x, y'-y)]}{\sqrt{\sum f(x',y')^2}\sqrt{\sum g(x'-x,y'-y)^2}} \tag{S2}$$

where $x = \ln(r)$, $y = \theta$ and $NCC(x,y)$ represents the normalized cross-correlation value at position (x,y), $f(x',y')$ represents the pixel values in the template image, and $g(x'-x, y'-y)$ represents the pixel values in the target image. This formula quantifies the similarity between the template and target images to determine the matching position of the template within the target image [5, 6]. Subsequently, with the center of the logarithmic polar coordinate image as the origin $(\ln(r_0), \theta_0)$, the scale ratio between the images can be obtained using the following equation [7]:

$$s = \frac{\ln(r_{\max}) - \ln(r_0)}{\ln(r_0)} \tag{S3}$$

where s represents the image scaling ratio. Therefore, based on the scaling ratio, the original ideal pupil can be scaled to achieve preliminary wavelength calibration. Subsequently, the PC operation is performed between the calibrated pupil and the actual pupil to achieve displacement correction [8], with the formula as follows:

$$PCC(x,y) = F^{-1}\left[\frac{\hat{f}(x,y)\hat{g}^{*}(x,y)}{\left|\hat{f}(x,y)\hat{g}(x,y)\right|}\right] \tag{S4}$$

where $PCC(x,y)$ represents the PC value at position (x,y), $\hat{f}(x,y)$ represents the Fourier transform of the corrected pupil, and $\hat{g}(x,y)$ represents the Fourier transform of the actual pupil. Then, the peak value $(x_{\max}, y_{\max})$ is obtained from it, and the position deviation can be calculated by:

$$\begin{cases} x_{shift} = x_{\max} - \frac{1}{2}M \\ y_{shift} = y_{\max} - \frac{1}{2}N \end{cases} \tag{S5}$$

where x_{shift} and y_{shift} represent the translation amounts along the x axis and y axis, respectively, M is the number of pixels along the x axis, and N is the number of pixels along the y axis. By sequentially calculating the spectrum corresponding to each LED, the offset distance from (x_{shift1}, y_{shift1}) to $(x_{shift28}, y_{shift28})$ of the pupil can be determined.

Table S1. Comparison on computational cost of LED calibration algorithms.

Methods \ Data	512×512 pixels	1024×1024 pixels	2048×2048 pixels
acIDT	23.7s	84.5s	239.8s
mcIDT	2.1s	7.5s	21.4s

As shown in Table. S1, it is worth mentioning that this algorithm has made significant improvements in computational speed compared to the LED array calibration algorithm based on the simulated annealing algorithm we proposed previously [9]. The computational efficiency has been increased by more than one order of magnitude, which greatly reduces the calibration time for the LED array.

3. SUPPLEMENTARY EXPERIMENT USING RESOLUTION TARGET

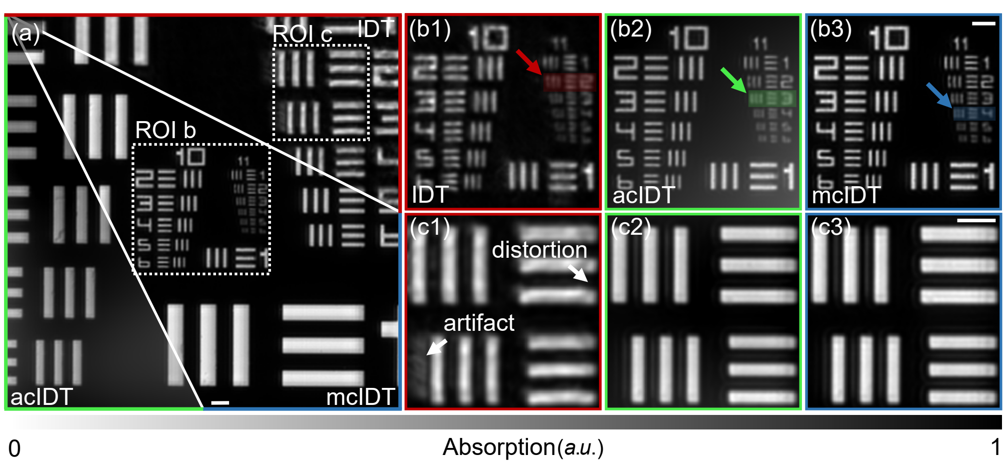

Fig. S3. Comparison of IDT results of resolution target. (a) Comparison of reconstructed 3D RI results under IDT, acIDT, and mcIDT methods when annular LED array position is deviated. (b)-(c) Enlarged images of the ROI b and c obtained under IDT, acIDT, and mcIDT methods respectively. Scale bar, (a,b,c) 2 μm.

To demonstrate the accuracy of the three-dimensional (3D) refractive index (RI) reconstruction using mcIDT method, we conducted experimental measurements on a 1951 USAF resolution target (Ready Optics Company, USA). Figure S3(a) shows the reconstruction results obtained using the conventional intensity diffraction tomography (IDT), algorithmically calibrated IDT (acIDT), and mcIDT methods under the condition of misalignment of the annular LED. To better compare the reconstruction performance of these three methods, we magnified the regions of interest (ROI) from Fig. S3(a), as shown in Figs. S3(b) and (c). It is evident that the conventional IDT, which lacks LED calibration, results in significant blurring in the reconstructed 3D RI, with the resolution markedly decreasing to 436 nm (Group 11, Element 2), accompanied by severe artifacts and distortions. Although the acIDT method can recover some image details, the issue of misalignment between the annular LED source and the optical axis persists, leading to unavoidable RI distortion (as indicated by the white dashed circles in the figure), and the resolution only reaches 388 nm (Group 11, Element 3), which falls short of the theoretical resolution limit of 345 nm. In contrast, the mcIDT method, which combines algorithmic "calibration" with physical "correction," significantly enhances the resolution of 3D RI reconstruction to 346 nm (Group 11, Element 4), very close to the theoretical resolution limit, thereby greatly improving the accuracy of the reconstruction results.

4. ANALYSIS OF ANNULAR LED PARAMETERS AND MICROSPHERE EXPERIMENTS

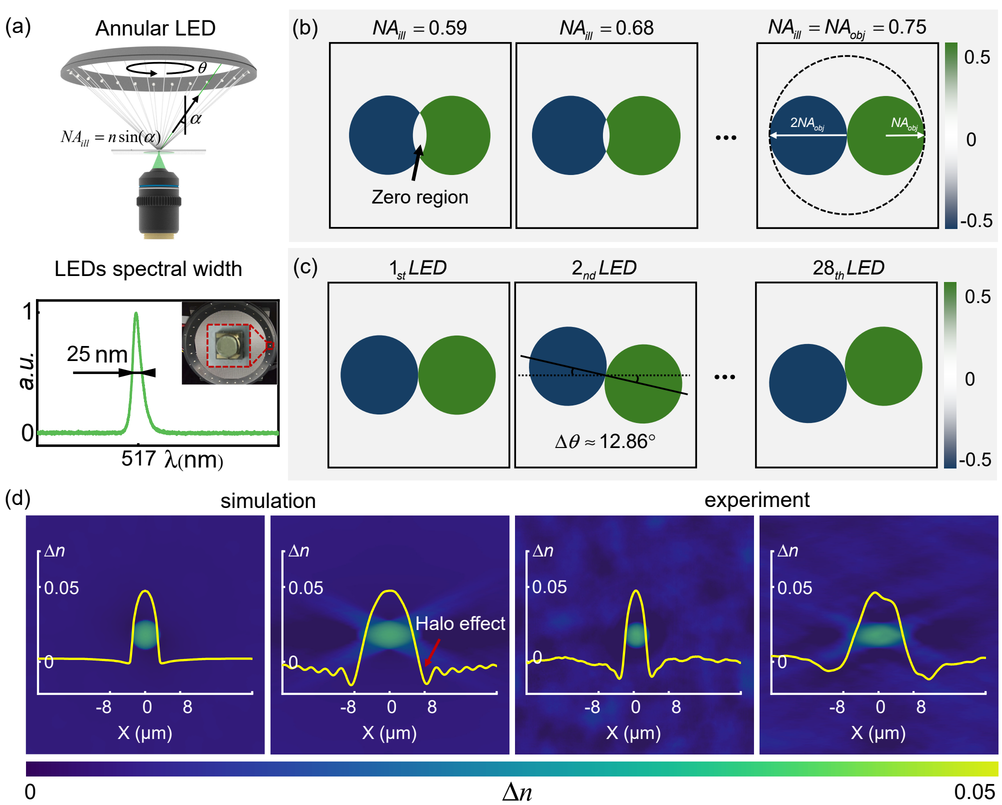

Fig. S4. Analysis of annular LED parameters and microsphere experiments. (a) Model of the annular LED and its emission wavelength. (b) Phase transfer functions corresponding to different illumination angles. (c) Phase transfer functions corresponding to different illumination NA. (d) Simulation and experiments of polystyrene microspheres.

As shown in Fig. S4(a), the illumination elements on the annular LED are sequentially activated to generate plane waves with a NA of 0.75 for multi-angle illumination. We calibrated the central wavelength and spectral bandwidth of the LED using a spectrometer (CCS200/M, Thorlabs) and obtained the spectral curve of the LED. Each LED provides quasi-monochromatic illumination with a central wavelength of 517 nm and a full width at half maximum (FWHM) of 25 nm. As shown in Fig. S4(b), when the annular LED is misaligned, the illumination NA of some LED elements decreases, causing the two pupils in the frequency domain to no longer perfectly tangent. The overlapping regions cancel each other out, leading to the loss of low-frequency information [10]. After correction, the LED center is coaxial with the optical axis, and the illumination NA matches the objective NA, as shown in Fig. S4(c). At this point, the two anti-symmetric pupils of the phase transfer function are in tangential contact, ensuring that both high-frequency and low-frequency phase information of the sample can be completely transferred to the intensity image. As shown in Fig. S4(d), to verify the quantitative three-dimensional refractive index reconstruction capability of the mcIDT method, we conducted experiments using polystyrene microspheres as test samples and compared the results with the simulation results of pure phase microspheres. Both experimental and simulated reconstructions were performed under consistent parameters to ensure the validity of our comparative analysis. The ideal microsphere with a 6 μm diameter and RI of 1.60, and it is immersed in a matched medium ($n_m = 1.518$, Olympus, Japan). By comparing the results, we found no significant differences between the experimental and simulated results. It should be noted that due to the limited range of incident angles in a single-objective system, certain spatial frequency components along the optical axis cannot be acquired, leading to the "missing cone problem" [11]. This issue not only reduces the axial resolution but also hinders the accuracy of refractive index reconstruction, causing energy leakage and oscillations at the edges of the reconstructed object, resulting in halo-like artifacts. This problem can be effectively addressed by using opposite illumination or deep learning methods [12, 13].

REFERENCES

1. S. Derrode and F. Ghorbel, "Robust and efficient fourier–mellin transform approximations for gray-level image reconstruction and complete invariant description," Comput. Vis. Image Underst. **83**, 57–78 (2001).
2. X. Wang, B. Xiao, J.-F. Ma, and X.-L. Bi, "Scaling and rotation invariant analysis approach to object recognition based on radon and fourier–mellin transforms," Pattern Recognit. **40**, 3503–3508 (2007).
3. S. Kumar, H. Azartash, M. Biswas, and T. Nguyen, "Real-time affine global motion estimation using phase correlation and its application for digital image stabilization," IEEE Transactions on Image Process. **20**, 3406–3418 (2011).
4. Y. S. Heo, K. M. Lee, and S. U. Lee, "Robust stereo matching using adaptive normalized cross-correlation," IEEE Transactions on Pattern Analysis Mach. Intell. **33**, 807–822 (2010).
5. A. Kaso, "Computation of the normalized cross-correlation by fast fourier transform," PloS One **13**, e0203434 (2018).
6. S. Liu, B. Yang, Y. Wang, *et al.*, "2d/3d multimode medical image registration based on normalized cross-correlation," Appl. Sci. **12**, 2828 (2022).
7. Y. Pu and C. Chen, "A comparison of cross-correlation-based and phase-correlation-based image registration algorithms for optical coherence tomographic angiography," Chin. Opt. Lett. **22**, 071101 (2024).
8. C. Dai, Y. Zheng, and X. Li, "Accurate video alignment using phase correlation," IEEE Signal Process. Lett. **13**, 737–740 (2006).
9. J. Sun, Q. Chen, Y. Zhang, and C. Zuo, "Efficient positional misalignment correction method for fourier ptychographic microscopy," Biomed. Opt. Express **7**, 1336–1350 (2016).
10. J. Sun, C. Zuo, J. Zhang, *et al.*, "High-speed fourier ptychographic microscopy based on programmable annular illuminations," Sci. reports **8**, 7669 (2018).
11. J. Lim, K. Lee, K. H. Jin, *et al.*, "Comparative study of iterative reconstruction algorithms for missing cone problems in optical diffraction tomography," Opt. express **23**, 16933–16948 (2015).
12. N. Zhou, J. Sun, R. Zhang, *et al.*, "Quasi-isotropic high-resolution fourier ptychographic diffraction tomography with opposite illuminations," ACS Photonics **10**, 2461–2466 (2023).
13. H. Chung, J. Huh, G. Kim, *et al.*, "Missing cone artifact removal in odt using unsupervised deep learning in the projection domain," IEEE Transactions on Comput. Imaging **7**, 747–758 (2021).